# Laser Directed Energy Deposition of Bulk 316L Stainless Steel

**Alessandro Ascari**[1] · **Adrian H. A. Lutey**[2] · **Erica Liverani**[1] · **Alessandro Fortunato**[1]

## Abstract

Laser directed energy deposition (DED) of high-density parallelepiped 316L stainless steel specimens has been performed while varying laser power, scanning velocity, powder mass flow rate and layer thickness. An extensive set of analyses has been performed into the resulting dimensions, surface roughness, microstructure, hardness, tensile strength, build substrate temperature, deposition efficiency, production time and specific energy input with the aim of differentiating variations in component performance and process efficiency for components that have already been optimized in terms of density. Average layer height is found to be an approximately linear function of the powder line mass flow rate, while samples with the same powder feed per unit length have similar microstructures despite differences in scanning velocity and total powder feed rate. The hardness of specimens is generally higher than bulk 316L stainless steel, while yield and ultimate tensile strength are similar or higher than the bulk material but with dependence on the load direction. Deposition efficiency is strongly influenced by the scanning strategy and laser off time, with values as low as 42% with a "raster" scanning strategy and up to 84% with a "snake" scanning strategy. The large number of analyses performed on high-density components provides important new insight into factors affecting build quality and process efficiency that go beyond simply maximizing density, suggesting that significant further improvements can be obtained. Such knowledge is exploitable for application-specific process optimization and implementation of open and closed-loop height control strategies for production of bulk 316L stainless steel components.

**Keywords** Additive manufacturing · Directed energy deposition · Laser · 316L stainless steel

---

✉ Alessandro Ascari
    a.ascari@unibo.it

Extended author information available on the last page of the article.

## Introduction

Use of laser technology as a heat source for deposition of metal and/or ceramic powders on metal substrates dates back more than thirty years. Scientific interest towards laser-based powder deposition techniques began with the purpose of identifying an alternative coating technology to flame and plasma deposition in generating wear-resistant layers on less noble metallic substrates [1–5]. In the years that followed, the potential of this technology pushed interest further with several studies devoted to metallurgy [6], process monitoring [7] and modeling [8]. Focus then moved towards new applications, process optimization for a large number of cladding powders and mixtures [9–11], deposition on substrates other than carbon steels [12–14] and the role of powder deposition equipment and powder stream behavior [15–17]. From the early 2000s, the large variety of laser sources available on the market moved attention towards newer and more flexible sources including Nd:YAG [18, 19] and diode lasers [20], as well as more complex applications such as repair [21] and hybrid manufacturing [22]. A completely new paradigm relating to laser directed energy deposition (DED) started to gain more interest [23, 24]. The most extensive studies during this period demonstrated fabrication of both thin-walled and bulk structures. In relation to the former, the most widely studied topics included the control of process parameters to build tall and defect-free hollow structures [25–29]. In relation to bulk structures, most works considered small samples, including deposition of narrow structures for stringers in AISI316 [30], production of thin cylinders for tensile tests [31], deposition of titanium alloy samples for tensile and fatigue testing [32], evaluation of Hot Isostatic Pressing (HIP) post-processing [33] and production of small blocks for evaluation of microstructure and mechanical performance [34, 35].

The resulting mechanical properties and microstructure of components produced by DED depend primarily on the applied energy density, powder feed rate, scanning strategy and layer thickness. The effects of these parameters and control strategies have been discussed extensively by Shamsaei et al. [36] in an overview of laser-based additive manufacturing processes. Insufficient laser power leads to components that are porous due to insufficient melting, while excessive laser power leads to uncontrolled thermal deformation and melt flow with formation of depressions and poor dimensional accuracy. In terms of processing strategies, raster, bi-directional, offset and fractal deposition patterns are commonly used. It has been shown that offset and fractal patterns produce smallest deformations, while raster patterns are most effective where lines are oriented 90° to the long axis of the part [37]. Layer thickness and the correct choice of vertical feed, $\Delta z$, are of fundamental influence on the process. The difference between the resulting layer thickness and $\Delta z$ must be as close to zero as possible to ensure that laser focus and powder dynamics are constant with respect to the surface being produced. In an open-loop configuration, the process is generally more sensitive to excessively high feed rates than low feed rates due to greater energy loss as the DED head becomes progressively further from the workpiece. The resulting layer thickness depends on parameters such as the powder feed rate, scanning speed, hatch spacing and number of layers, for which correct selection of the vertical feed rate is a complex task that must be optimized experimentally prior to implementation of closed-loop control strategies.

To overcome issues relating to layer height, several studies have proposed measurement systems and adaptive deposition strategies with closed-loop control of parameters such as laser power, scanning speed, process time intervals and hatch spacing [36, 38]. Song et al. [39] implemented a feedback control system utilizing three high-speed CCD cameras for triangulation and a two-color pyrometer to monitor melt pool height and temperature, avoiding over- and under-building with a rule-based master height controller and slave temperature controller for adaptive laser power output. By producing turbine blades in AISI316L with and without active control, they showed that the system could effectively compensate for variations in heat accumulation due to workpiece geometry. More recently, Donadello et al. [40] proposed a system for height monitoring employing a probe laser beam and coaxial camera to determine the mismatch between the programmed and actual build height. By applying the system while building a 35 mm diameter hollow cylinder in AISI316L, the authors were able to observe and quantify self-regulating mechanisms taking place due to variations in melt pool dynamics and powder-laser interactions throughout the process, thus proposing potential future approaches for identification of optimal processing conditions.

The resulting microstructure and residual stresses following DED are strongly dependent on the thermal history during the build [36]. Of the various materials employed in additive manufacturing, AISI316 and AISI316L have seen extensive investigation due to their wide range of applications, excellent mechanical properties and ease of processing. Cooling rates in the order of $10^2\,K/s$ during DED lead to columnar grains with widths in the order of $40 - 100\,\mu m$ and lengths in the order of $500 - 2500\,\mu m$ [41]. The imposed thermal heating and cooling cycles create a fine, complex microstructure with austenite growing epitaxially from previously deposited material at layer boundaries, leading to improved mechanical properties compared to the wrought material [42, 43]. Works analyzing the porosity, density and defects of AISI316L stainless steel blocks produced via DED have found that the track width changes from the bottom to the top of the object due to changes in thermal gradient, while larger grain sizes are generally observed within the track body and oxides along fusion lines [44]. An extensive overview of the effects of processing strategies and parameters on DED outcomes for AISI316L is provided by Saboori et al. [43], where thermal history, microstructure and mechanical properties are shown to depend strongly on build parameters. Powder quality and build atmosphere are also highlighted as factors influencing oxide and non-metallic inclusions, ultimately affecting mechanical properties.

While a large volume of literature evaluates DED build quality in terms of dimensional accuracy and density, the present work evaluates the effects of process parameters and deposition strategies on a wider range of outcomes for industrially-relevant high-density AISI316 specimens, including the resulting dimensions, density, surface roughness, microstructure, hardness, tensile strength, build substrate temperature, deposition efficiency, production time and specific energy input. The analysis is specifically aimed at differentiating variations in component performance and process efficiency for large samples whose density has already been maximized. Optimization of process parameters is an essential step for obtaining defect-free components [43], for which new insight gained into factors affecting build quality is

exploitable for application-specific process optimization and implementation of open and closed-loop height control strategies for production of bulk 316L stainless steel components.

## Experimental Procedure

The deposition scanning strategy employed for producing specimens consisted of a single deposition pass along the perimeter of each layer followed by parallel-line infill passes. The infill scanning direction was rotated 90° clockwise with each successive layer. Two different infill scanning strategies were applied; the first involved returning the DED head to the same starting edge for all lines within a given layer; the second involved scanning adjacent lines in alternating directions. These "raster" and "snake" scanning strategies are presented schematically in Figs. 1 and 2. In both cases, movement between the end of a given line and the start of the next was performed with rapid movement of the DED head and no laser emission; however, powder emission continued due to limitations in the response time of the powder supply system. Laser power was set to an initial value of $P$ for the first layer and decreased with each subsequent layer by $\Delta P$ until reaching a minimum value of $P_{min}$. For the raster scanning strategy, laser power was increased by 300 $W$ for 0.5 $s$ at the start of each pass to ensure complete melting of the initial part of each deposition line. Several process parameters were held constant following previous optimization, including the hatch spacing, rapid movement velocity, transport and shielding gas type and volume flow rate, laser spot diameter, stand-off distance and powder injector diameter. All constant values are presented in Table 1.

The hardware system used in this campaign was based on the equipment reported in Fig. 3 and Table 2.

A first set of preliminary tests was performed by producing parallelepipeds over as wide a range of operating parameters as possible with the aim of optimizing build
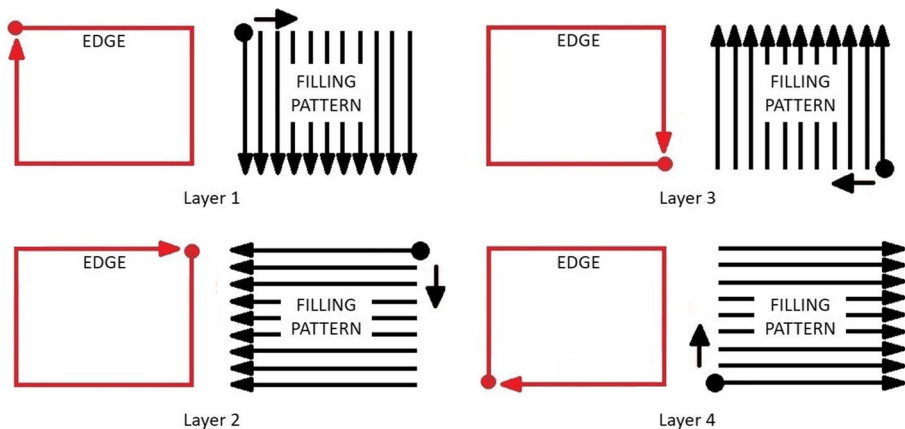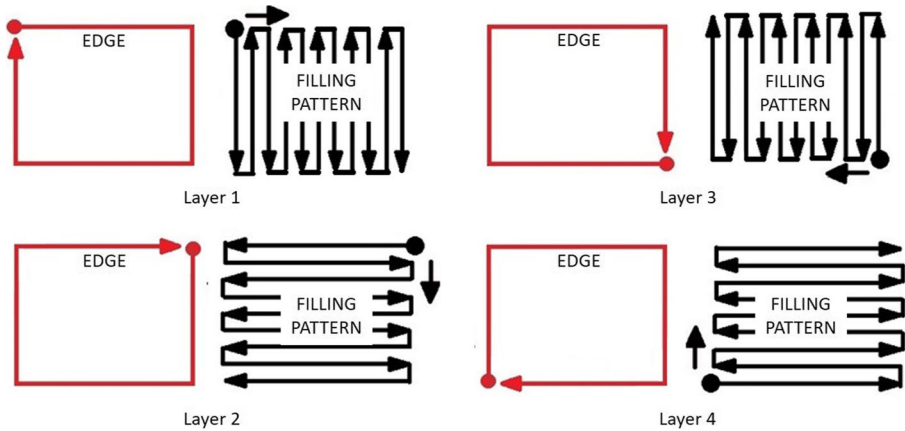


**Fig. 1** Raster scanning strategy employed to produce parallelepipeds

**Fig. 2** Snake scanning strategy employed to produce parallelepipeds

density and dimensional accuracy. The nominal base area was $20 \times 40 \, mm$ for each layer, leading to samples with a base size slightly larger in both directions due to the width of deposition lines. For the sake of simplicity, only combinations leading to the best outcomes amongst these preliminary tests will be presented here within. Parameters that were varied during these tests are given in Table 3, including the powder feed rate ($\dot{m}$), scanning velocity ($V$), $\Delta z$, $P$, $\Delta P$, $P_{min}$, scanning strategy and number of layers ($n$). The powder feed per unit length (deposition rate) ($\hat{m}$) was calculated by dividing the powder feed rate by the scanning velocity ($\hat{m} = \dot{m}/V$).

Based on the results of the aforementioned preliminary tests, a second set of experiments was performed over a more limited parameter range to produce parallelepiped samples for complete process characterization. The idea behind the choice of process parameters in this case (see Table 4) was to select only the maximum and minimum powder feed rate so that only domain boundaries were tested. Two different nominal base areas were employed, $26 \times 96 \, mm$ and $27 \times 31 \, mm$, respectively, with the resulting base sizes being slightly larger due to the width of each deposition line. The number of layers was chosen to achieve approximately the same geometry in all cases based on the powder feed rate and average layer thickness obtained during preliminary tests, noting that all specimens were to have sufficient stock to allowing machining of tensile test specimens to standardized dimensions. The parallelepipeds with larger base size were referred to as having horizontal orientation, while those

| **Table 1** Constant process parameters | | |
|---|---|---|
| | Hatch spacing | $1 \, mm$ |
| | Rapid movement velocity | $50 \, mm/s$ |
| | Transport gas | Argon ($7.5 \, L/min$) |
| | Shielding gas | Argon ($20 \, L/min$) |
| | Laser spot diameter | $2.3 \, mm$ |
| | Stand-off distance | $25 \, mm$ |
| | Powder injector diameter | $1 \, mm$ |
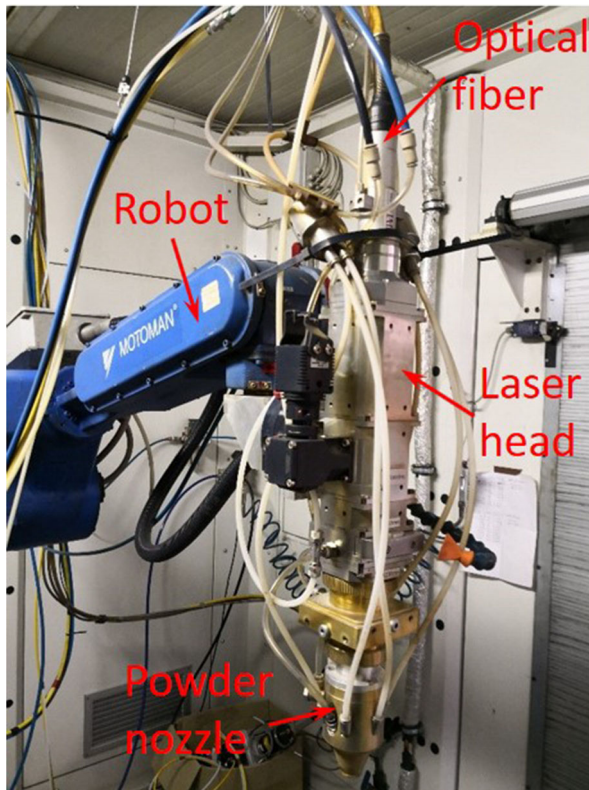
**Fig. 3** Photograph of experimental equipment

with smaller base size were referred to as having vertical orientation. Values of $\Delta z$ and laser power were maintained similar to the preliminary tests, with minor corrections to ensure that the $\Delta z$ error was as low as possible but always positive to avoid an increase in the distance between the DED head and workpiece. Values of $\Delta z$ were

| Table 2 Experimental equipment characteristics | | |
|---|---|---|
| | Laser source | Laserline LDF 4000-30 |
| | Beam quality (BPP) | 30 mm·mrad |
| | Collimator focal length | 82 mm |
| | Focusing lens focal length | 300 mm |
| | Fiber core diameter | 600 $\mu$m |
| | Theoretical spot diameter | ≈2.25 mm |
| | Powder nozzle | GTV 6-Way |
| | Powder feeder | GTV PF 2/2 |
| | Powder spot | ≈2 mm |
| | Standoff distance | 25 mm |

**Table 3** Preliminary test parameters leading to best outcomes

| Test | $\dot{m}$ [g/min] | $V$ [mm/s] | $\hat{m}$ [mg/mm] | $\Delta z$ [μm] | $P$ [W] | $\Delta P$ [W] | $P_{min}$ [W] | Scan.* | $n$ |
|------|------|------|------|------|------|------|------|------|------|
| 1A | 9.1 | 17 | 8.9 | 1300 | 2300 | 75 | 1800 | R | 18 |
| 1B | 9.1 | 17 | 8.9 | 1300 | 2300 | 75 | 1800 | R | 22 |
| 2A | 9.1 | 17 | 8.9 | 1200 | 2000 | 75 | 1500 | S | 18 |
| 2B | 9.1 | 17 | 8.9 | 1200 | 2000 | 75 | 1500 | S | 21 |
| 3A | 11.9 | 17 | 11.7 | 1650 | 2500 | 75 | 2000 | S | 15 |
| 3B | 11.9 | 17 | 11.7 | 1650 | 2500 | 75 | 2000 | S | 16 |
| 4A | 14.6 | 17 | 14.3 | 2000 | 2700 | 75 | 2200 | S | 10 |
| 4B | 14.6 | 17 | 14.3 | 2000 | 2700 | 75 | 2200 | S | 14 |
| 5A | 9.1 | 27 | 5.6 | 800 | 2200 | 100 | 1500 | S | 25 |
| 5B | 9.1 | 27 | 5.6 | 800 | 2200 | 100 | 1500 | S | 33 |
| 6A | 11.9 | 27 | 7.3 | 1000 | 2500 | 100 | 1500 | S | 25 |
| 6B | 11.9 | 27 | 7.3 | 1000 | 2500 | 100 | 1500 | S | 27 |
| 7A | 14.6 | 27 | 9.0 | 1300 | 3000 | 100 | 1700 | S | 18 |
| 7B | 14.6 | 27 | 9.0 | 1300 | 3000 | 100 | 1700 | S | 21 |

*R = Raster scanning, S = Snake scanning

generally lower for samples with vertical orientation than those with horizontal orientation using the same process parameters due to the larger number of layers to be produced in the former case and consequent tendency to achieve a lower average layer thickness. The required value of $P_{min}$ was also lower for vertical samples than for horizontal samples due to the smaller interface area with the base and therefore lower thermal conduction losses.

**Table 4** Characterization test parameters varied during tests

| Test | Orient.* | $\dot{m}$ [g/min] | $V$ [mm/s] | $\hat{m}$ [mg/mm] | $\Delta z$ [μm] | $P$ [W] | $\Delta P$ [W] | $P_{min}$ [W] | Scan.* | $n$ |
|------|------|------|------|------|------|------|------|------|------|------|
| 1M | H | 9.1 | 17 | 8.9 | 1150 | 2300 | 75 | 1800 | R | 30 |
| 2M | V | 9.1 | 17 | 8.9 | 1050 | 2300 | 75 | 1600 | R | 95 |
| 3M | H | 9.1 | 17 | 8.9 | 1200 | 2000 | 75 | 1500 | S | 28 |
| 4M | V | 9.1 | 17 | 8.9 | 1100 | 2000 | 75 | 1300 | S | 88 |
| 5M | H | 14.6 | 17 | 14.3 | 2000 | 2700 | 75 | 2200 | S | 18 |
| 6M | V | 14.6 | 17 | 14.3 | 1800 | 2700 | 75 | 1900 | S | 55 |
| 7M | H | 9.1 | 27 | 5.6 | 700 | 2200 | 100 | 1500 | S | 49 |
| 8M | V | 9.1 | 27 | 5.6 | 700 | 2200 | 100 | 1400 | S | 131 |
| 9M | H | 14.6 | 27 | 9.0 | 1100 | 3000 | 100 | 1700 | S | 32 |
| 10M | V | 14.6 | 27 | 9.0 | 1050 | 3000 | 100 | 1500 | S | 91 |

*H = Horizontal, V = Vertical, R = Raster scanning, S = Snake scanning

## Sample Analysis

Several equally-spaced measurements were performed between parallel faces on each sample with calipers to determine the average dimensions of each specimen with an accuracy of $\pm 0.05\,mm$. The average deviation in base geometry was evaluated as the average difference between the dimensions of the scanned area and the length and width of each sample. The average layer height was calculated based on the build height and total number of layers. This value was compared with $\Delta z$ to determine the feed rate error, which was defined as being positive when the average layer height was greater than the feed rate. Density measurements were performed with Archimedes' method for all samples with precision electronic scales. Three measurements were performed for each specimen, with average values expressed as a percentage of the bulk density of 316L stainless steel, $8.00\,g/cm^3$. For microstructural analysis, samples were mounted in phenolic resin and mirror polished prior to etching with Vilella's reagent and image capture with an optical microscope.

The surface topography of lateral sample surfaces perpendicular to the build plane was acquired with a Taylor Hobson Talysurf optical profiler with $10\times$ objective for the first set of tests, from which representative areal surface roughness parameters were calculated. After milling to a depth of $2\,mm$, HRA hardness tests (EN-ISO 6508) were performed on samples from the second set of tests along the center of the largest lateral face at regular intervals in the vertical direction. By determining the hardness along the entire height of each sample, it was possible to determine the average hardness and uniformity of the resulting hardness profile. The locations of hardness tests are shown schematically in Fig. 4. Tensile tests were performed on samples that had been machined to the standard geometry defined in ISO 6892-1:2016, shown in Fig. 5. Tests were performed with an Instron 8032 machine with a deformation rate of $0.00025\,s^{-1}$ as per the aforementioned standard. The yield strength was calculated based on the point at which each sample reached 0.2 % permanent deformation, while the ultimate tensile strength was based on the maximum load.
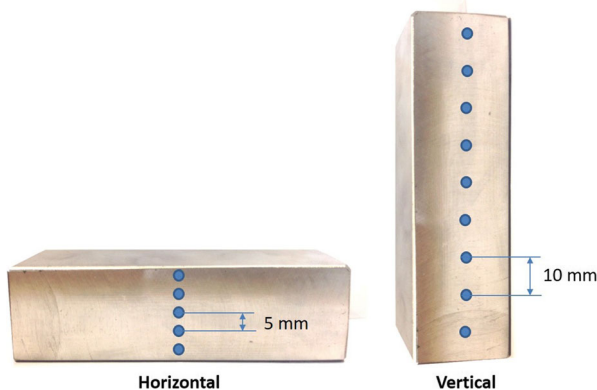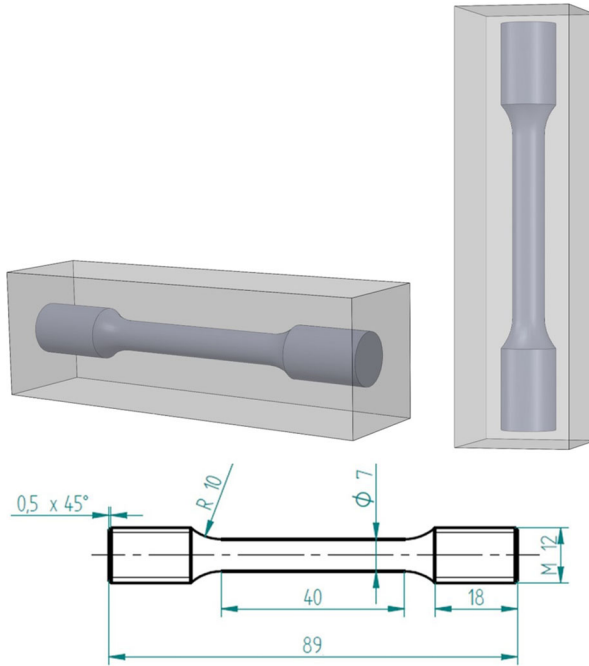


**Fig. 4** Locations of hardness tests performed on machined samples

**Fig. 5** Representation of tensile test sample

A number of process variables were monitored during production of the second set of samples, including the substrate temperature, deposition efficiency, production time and specific energy input. The substrate temperature was monitored with $1\,mm$ diameter K-type thermocouples placed in two $1.25\,mm$-diameter, $10\,mm$-deep holes drilled at the center of the largest and smallest lateral faces of the base, as shown in Fig. 6.
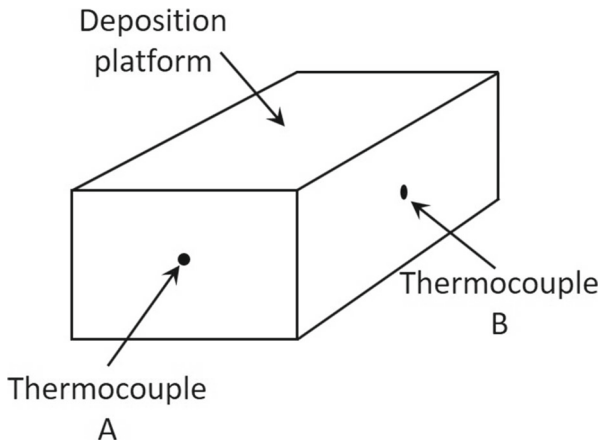


**Fig. 6** Positions of thermocouples on the platform

Deposition efficiency ($D_{eff}$, see Eq. 1) was calculated based on the mass of supplied powder ($m_{ps}$) and the mass of powder lost during the process ($m_{pl}$), which was recovered and weighed after each test with precision electronic scales.

$$D_{eff} = \frac{m_{ps} - m_{pl}}{m_{ps}} \cdot 100 \tag{1}$$

Production time was recorded for all samples and divided by the total deposited mass to calculate the deposition time required per unit mass. Finally, specific energy input was calculated based on the average laser power and deposited mass. This parameter allowed evaluation of the most energy-efficient deposition strategy, noting that all parameter combinations in the second group of tests resulted in high-density components.

## Results and Discussion

The dimensions, average layer height, average deviation in base geometry, vertical feed rate error, density and lateral surface average areal roughness of the best results obtained during preliminary tests are summarized in Table 5. The error in $\Delta z$ was no more than 0.08 $mm$ per layer in all cases, within the range reported in other studies employing online height monitoring systems [40], while the actual base dimensions were $2.0 - 3.6\,mm$ larger than the scanned dimensions due to the width of each deposited line. The density of all samples was greater than 99% in all cases. The average areal surface roughness ($S_a$) of lateral surfaces perpendicular to the build plane

**Table 5** Dimensions, density and average surface roughness of best results obtained during preliminary tests

| Test | Dimensions (W × L × H) [$mm$] | Av. layer height [$mm$] | Av. base error [$mm$] | $\Delta z$ error [$mm$] | Density [%] | Lateral $S_a$ [$\mu m$] |
|------|------|------|------|------|------|------|
| 1A | 22.8 × 42.5 × 23.2 | 1.29 | 2.6 | -0.01 | 99.3 | 91.5 |
| 1B | 22.5 × 42.8 × 29.4 | 1.34 | 2.6 | 0.04 | 99.3 | 47.8 |
| 2A | 22.6 × 42.8 × 23.0 | 1.28 | 2.7 | 0.08 | 99.4 | 25.1 |
| 2B | 22.2 × 41.8 × 25.6 | 1.22 | 2.0 | 0.02 | 99.4 | 40.1 |
| 3A | 23.2 × 43.3 × 25.2 | 1.68 | 3.2 | 0.03 | 99.4 | 37.8 |
| 3B | 23.1 × 43.1 × 25.4 | 1.59 | 3.1 | -0.06 | 99.4 | 47.9 |
| 4A | 23.4 × 43.9 × 20.2 | 2.02 | 3.6 | 0.02 | 99.3 | 36.3 |
| 4B | 23.4 × 43.4 × 28.2 | 2.01 | 3.4 | 0.01 | 99.3 | 74.2 |
| 5A | 22.0 × 41.7 × 21.8 | 0.87 | 1.8 | 0.07 | 99.4 | 19.6 |
| 5B | 22.5 × 42.7 × 27.2 | 0.82 | 2.6 | 0.02 | 99.4 | 19.9 |
| 6A | 22.2 × 41.8 × 26.6 | 1.06 | 2.0 | 0.06 | 99.3 | 19.5 |
| 6B | 22.3 × 42.1 × 28.7 | 1.06 | 2.2 | 0.06 | 99.3 | 22.7 |
| 7A | 22.8 × 42.4 × 24.2 | 1.34 | 2.6 | 0.04 | 99.3 | 32.9 |
| 7B | 22.7 × 42.6 × 26.5 | 1.26 | 2.6 | -0.04 | 99.3 | 30.0 |

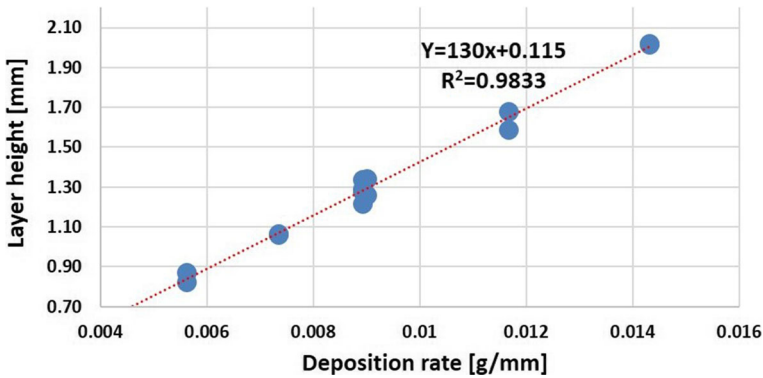**Fig. 7** Average layer height as a function of line deposition rate for the results in Table 5

ranged from $19.5\,\mu m$ to $91.5\,\mu m$, with values generally lower for the snake scanning strategy with lower scanning velocity and powder feed rate. Previous works have reported roughness values in the range $30 - 80\,\mu m$ and dependence on the scanning strategy [45], confirming that as-built surface quality is strongly dependent on the processing conditions employed. These results show that high density components with good dimensional accuracy can be achieved over a relatively wide operating range in terms of powder feed rate, scanning velocity, laser power and scanning strategy, provided that the deposited energy density is chosen correctly. The average layer height is presented as a function of the powder feed per unit length in Fig. 7. Noting the constant hatch spacing ($1\,mm$), the average layer height is an approximately linear function of $\hat{m}$ over the given parameter range, with no apparent difference between the raster and snake scanning strategies (Figs. 1 and 2). Similar dependence of layer height on $\hat{m}$ has been reported in other works for single layers of much lower thickness [46].

Samples 5M to 8M produced during the second set of tests are presented in Fig. 8. Despite their similar form, it is possible to observe differences in the characteristics of each parallelepiped depending on their orientation and layer thickness. Differences in the morphology of the external surfaces with changes in the powder feed per unit
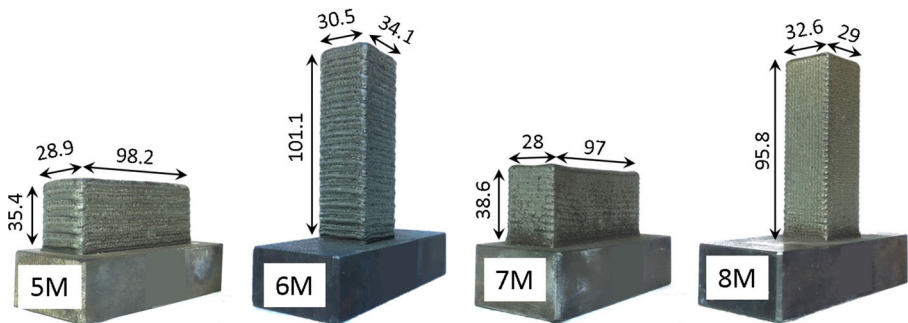


**Fig. 8** Samples 5M to 8M produced during second set of tests (dimensions in [mm])

length are evident, particularly when comparing specimens 5M and 6M, produced with $\hat{m} = 14.3\,mg/mm$, to specimens 7M and 8M, produced with $\hat{m} = 5.6\,mg/mm$.

Table 6 presents the dimensions, average layer height, average deviation in base geometry, vertical feed rate error and density of samples produced during the second set of tests. Deviation in base geometry is within the range $1.5 - 3.3\,mm$ and generally increases with increasing powder feed per unit length based on the total powder feed rate (increasing) and scanning velocity (decreasing). This outcome is due to the size of the melt pool during deposition, which increases as laser power is increased to deal with higher powder feed rate or as velocity is decreased and heat accumulation becomes more severe. A larger melt pool size results in greater fluidity and therefore greater lateral dispersion of material [39]. The average deviation in base geometry also tends to be higher for samples with vertical orientation than horizontal orientation due to the smaller base area in the former case and therefore greater heat accumulation and more frequent adjacent line passes. The error in $\Delta z$ remains within the range $0.00 - 0.10\,mm$ per layer in all cases, within the range reported in other studies [40]. The average layer height is shown as a function of $\hat{m}$ in Fig. 9. As with the preliminary tests and in other works [46], the average layer height is an approximately linear function of the powder line mass flow rate over the entire tested parameter range. There is nonetheless a slight reduction in average layer height for specimens with vertical orientation compared to horizontal orientation due to the greater number of layers. There is again no apparent difference between specimens produced with raster and snake scanning strategies. The measured density is greater than 99% in all cases, indicating correct choice of process parameters, particularly in relation to the laser power profile.

The microstructures of selected samples from the second test group are presented in Figs. 10 and 11 for horizontal and vertical orientations, respectively, and various positions and powder line mass flow rates. Only the upper zone of each horizontal sample is presented, while both upper and lower zones are instead presented for

Table 6 Dimensions and density of samples produced during second test group

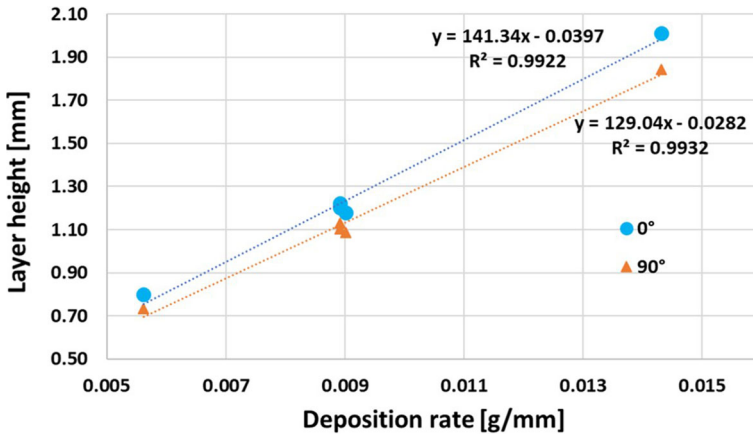| Test | Dimensions (W × L × H) [mm] | Av. layer height [mm] | Av. Base error [mm] | $\Delta z$ error [mm] | Density [%] |
|------|------|------|------|------|------|
| 1M | 28.3 × 98.0 × 35.9 | 1.22 | 2.2 | 0.07 | 99.02 |
| 2M | 29.6 × 33.5 × 104.8 | 1.10 | 2.6 | 0.05 | 99.14 |
| 3M | 28.0 × 97.3 × 32.4 | 1.20 | 1.7 | 0.00 | 99.08 |
| 4M | 30.0 × 33.7 × 99.2 | 1.13 | 2.9 | 0.03 | 99.19 |
| 5M | 28.9 × 98.2 × 35.4 | 2.01 | 2.6 | 0.01 | 99.12 |
| 6M | 30.5 × 34.1 × 101.1 | 1.84 | 3.3 | 0.04 | 99.05 |
| 7M | 28.0 × 97.0 × 38.6 | 0.80 | 1.5 | 0.10 | 99.13 |
| 8M | 29.0 × 32.6 × 95.8 | 0.73 | 1.8 | 0.03 | 99.13 |
| 9M | 28.3 × 97.3 × 37.0 | 1.18 | 1.8 | 0.08 | 99.03 |
| 10M | 29.2 × 33.0 × 98.6 | 1.09 | 2.1 | 0.04 | 98.93 |

**Fig. 9** Average layer height as a function of line deposition rate for second test group

vertical samples due to their larger height. Both parallel and perpendicular laser passes are evident in the images, with clear distinction of the melt zone in each case. These characteristics are typical of bulk AISI316L samples produced via DED [45], with dendritic microstructures at the edge of the melt pool and epitaxial growth from the preceding solid interface [42]. With reference to the samples with horizontal orientation, it can be seen that the melt pool size increases with powder feed
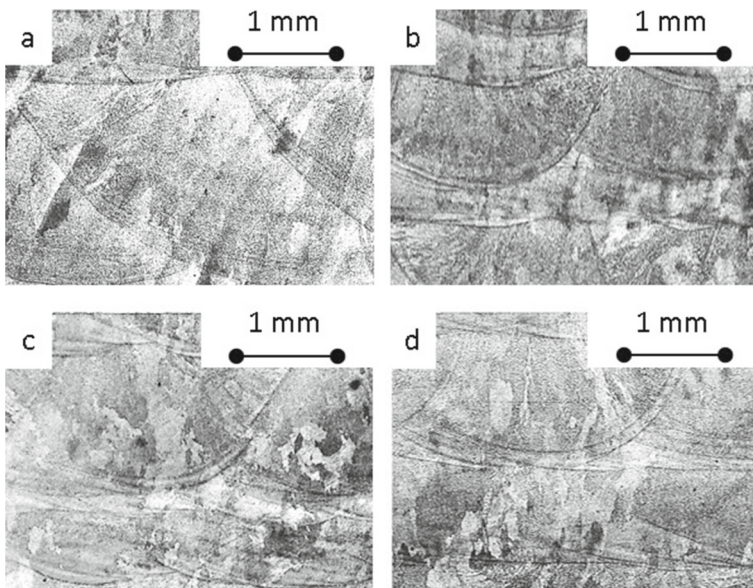


**Fig. 10** Comparison of microstructures obtained with horizontal sample orientation and variations in powder line mass flow rate (**a**) 5M (14.3 $mg/mm$) upper zone; (**b**) 7M (5.6 $mg/mm$) upper zone; (**c**) 3M (8.9 $mg/mm$) upper zone; (**d**b) 9M (9.0 $mg/mm$) upper zone
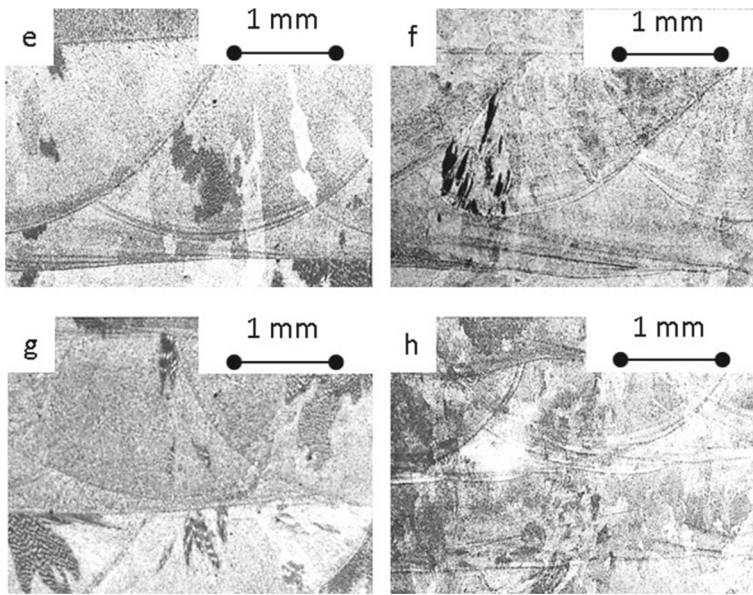
**Fig. 11** Comparison of microstructures obtained with vertical sample orientation and variations in position and powder line mass deposition rate (**a**) 6M (9.0 $mg/mm$) upper zone; (**b**) 6M (9.0 $mg/mm$) lower zone; (**c**) 8M (5.6 $mg/mm$) upper zone; (**d**) 6M (5.6 $mg/mm$) lower zone

per unit length ($\hat{m}$) (Fig. 10 (a) and (b)), while samples obtained with the same value of $\hat{m}$ have similar microstructures despite differences in scanning velocity and total powder feed rate (Fig. 10 (c) and (d)). The resulting microstructure is therefore relatively insensitive to the scanning velocity and total powder feed rate at constant powder feed per unit length. In relation to samples with vertical orientation (Fig. 11), it is instead evident that initial layers tend to have reduced dimensions compared to upper layers within the same sample. This effect is due to a gradual reduction in thermal conduction losses to the build platform as the build height increases.

Figure 12 displays the hardness of samples from the second test group as a function of the distance from the build platform. It is evident that only relatively minor variations in hardness take place along the height of each individual sample. Hardness values are generally higher than those of bulk 316L stainless steel (81 HB, approximately 50 HRA) due to the thermal cycle induced during DED. While the results are similar in magnitude to measured values in other works for bulk AISI316L, reported as approximately 173-198 HV in [44] depending on indentation location, 175-255 HV in [41] depending on laser spot size and 185-235 HV in [27] depending on layer number, the current results highlight important variations depending on part geometry. Samples produced with horizontal orientation are characterized by higher hardness than samples produced with vertical orientation due to the larger available area for thermal conduction in the former case and therefore higher cooling rates.
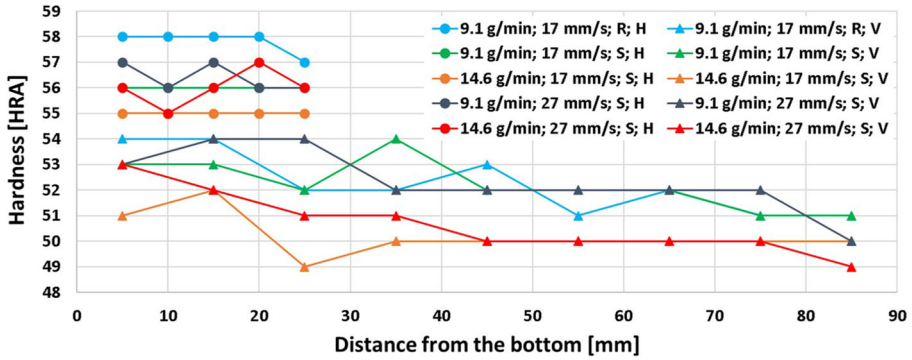
**Fig. 12** Hardness measurements on all samples in the second test group. The legend reports: powder feed rate; deposition speed; scanning strategy; specimen orientation

Horizontal samples produced with a raster scanning strategy exhibit the highest hardness, again due to the high cooling rate, which is accentuated in this case as the laser does not emit for longer periods between each deposition line.

The yield and ultimate tensile strength of samples from the second test group are given in Fig. 13, together with reference values for bulk 316L stainless steel. Columns filled with solid color refer to horizontal specimens, while dashed columns refer to vertical specimens. Results for sample 2M are not presented due to damage
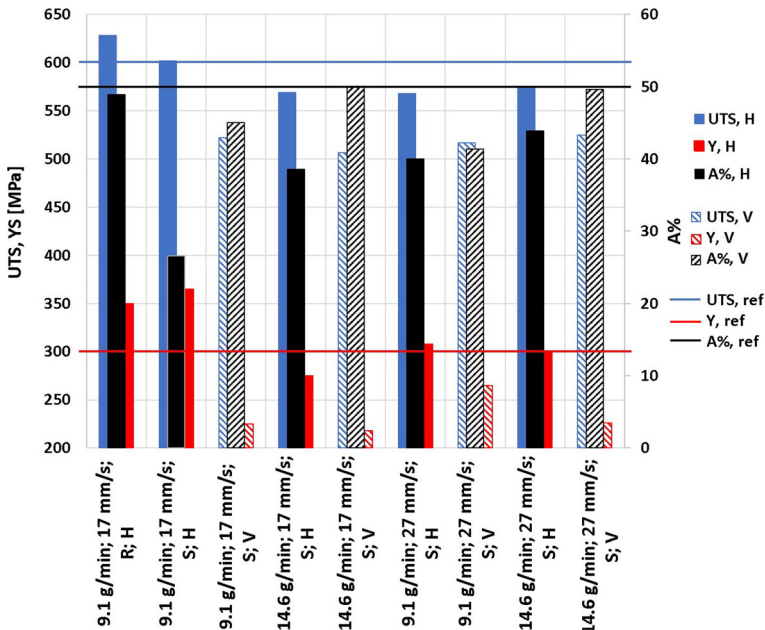


**Fig. 13** Yield and ultimate tensile strength of all samples in the second test group. The horizontal axis labels report: powder feed rate; deposition speed; scanning strategy; specimen orientation

that occurred during the machining phase. The yield and ultimate tensile strength of samples produced by DED are similar and in some cases higher than the bulk material, consistent with the findings of previous studies [42, 43]. While values of yield and ultimate tensile strength are similar in magnitude to those reported in the literature, where dependence on laser spot size and energy density has been observed [41], the present study highlights important variations due to the laser scanning strategy and sample geometry. Energy density is defined as $E = P/(V \cdot d)$, where $P$ is the laser power, $V$ the deposition speed and $d$ the average track width [41]. Highest strength was obtained with sample 1M, which was likely due to the high cooling rates obtained with the raster scanning strategy. The tensile and yield strength both tended to be lower for samples with vertical orientation, where the load was applied perpendicular to the build plane, than those with horizontal orientation, where the load was applied parallel to the build plane. The elongation instead tended to increase with a higher powder feed rate, as well as for samples with vertical orientation. No correlation between the density and yield or ultimate tensile strength was observed, which was likely due to the high density of all samples. Fig. 14 instead presents the same parameters as a function of the average HRA hardness, where it is clear that higher hardness generally results in higher strength.

The substrate temperature profile measured by thermocouples located at the center of the largest and smallest lateral faces of the base during production of sample M6 are presented in Fig. 15. It can be seen that the substrate temperature gradually increased with progressive material deposition up to a maximum, after which the height of the specimen and thermal dispersion prior to the base led to a gradual reduction in base temperature. This decrease was faster for samples with vertical orientation due to faster vertical growth of the specimen and lower surface area at the interface between the specimen and base. The temperature at the center of the largest lateral face was always higher than that of the smallest face due to the greater distance of the latter from the specimen. The maximum substrate temperature for production of all samples in the second test group is presented as a function of process parameters in Fig. 16. The maximum temperature was lower for samples with vertical orientation than horizontal orientation. The results show relatively strong dependence on the powder feed rate, as an increase in this parameter from 9.1 $g/min$



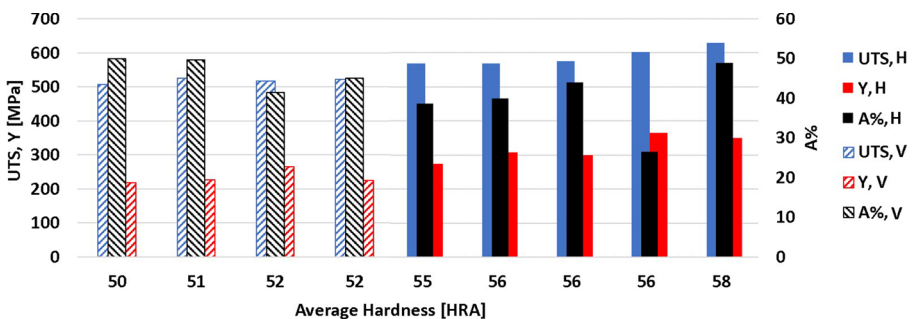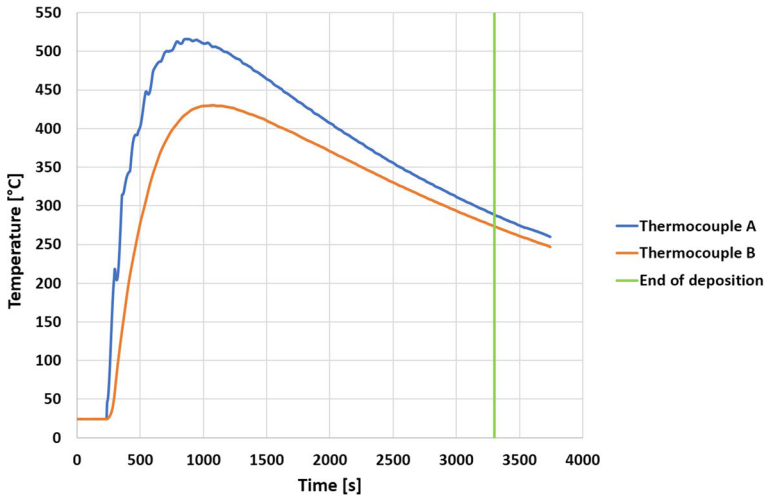**Fig. 14** Yield and ultimate tensile strength as functions of average hardness

**Fig. 15** Temperature profiles of sample M6 with vertical orientation

to 14.6 $g/min$ requires higher laser power. There are instead no discernible trends in relation to the scanning velocity or use of a raster or snake scanning strategy.

Deposition efficiency is presented in Fig. 17 as a function of powder feed rate and scanning velocity for the second test group. This parameter was essentially related to the total distance that the DED head had to travel between deposition lines. It must be noted that no laser emission took place during rapid movement between the end of each line and the start of the next; however, powder emission continued
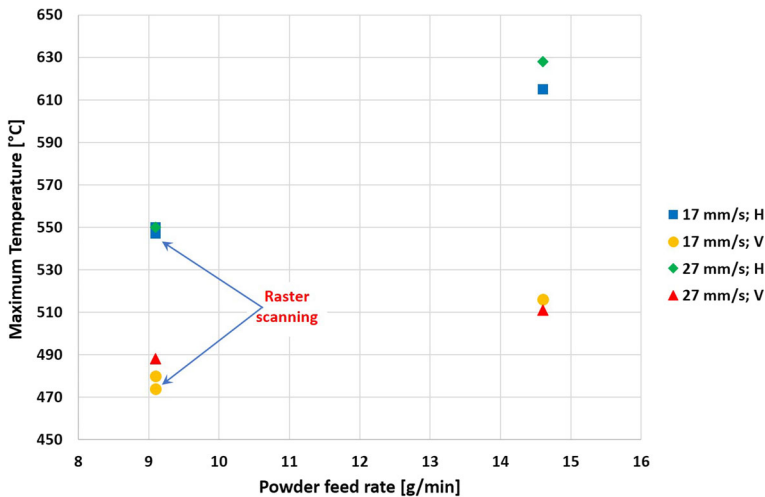


**Fig. 16** Maximum base temperature as a function of powder feed rate and scanning velocity for second test group
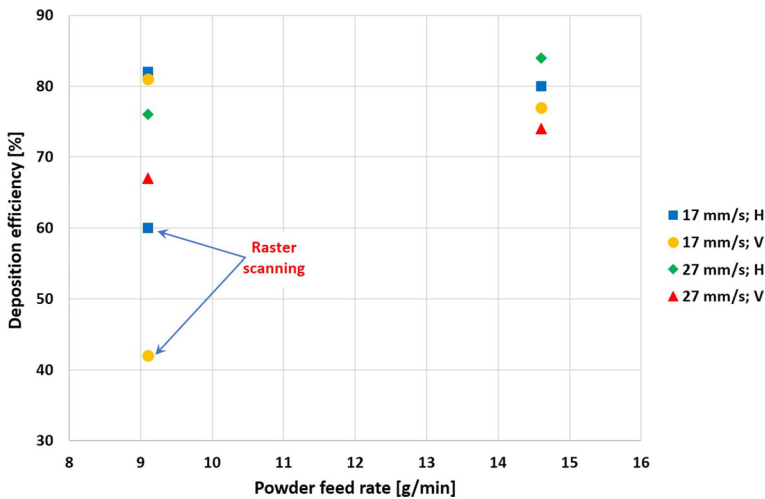
**Fig. 17** Deposition efficiency as a function of powder feed rate and scanning velocity for second test group

during this phase as system response was not sufficiently fast to allow interruption in supply. Lowest deposition efficiency was therefore obtained with a raster scanning strategy due to the large return distance to the same starting edge of each line within a given layer. In the case of a snake scanning strategy, deposition efficiency was a function of the ratio between the total deposited volume and the total number of lines. Worse results were achieved with a scanning velocity of $27\,mm/s$ that at $17\,mm/s$, all other parameters being constant, as the layer thickness was lower requiring a greater total number of deposition lines. Similarly, samples with vertical orientation achieved lower deposition efficiency than those with horizontal orientation due to the shorter average line length and therefore greater number of lines. Higher efficiency would be expected with more rapid movement between each deposition line. Values above 75 % are nonetheless higher than those reported in the literature [47, 48], indicating that correct choice of the scanning strategy can drastically improve deposition efficiency. The relatively large difference between maximum and minimum values of deposition efficiency highlights the problem of powder waste under certain process conditions despite high build quality. Recycling of unused powder is highly advisable, with further investigation required into treatment methods for powder recycling and improved reusability for industrial DED processes.

Actual deposition rate is presented in Fig. 18 as a function of powder feed rate and scanning velocity. This parameter is calculated as the ratio between the actual deposited mass and the actual deposition time.

Finally, the specific energy of deposition is presented in Fig. 19, calculated by dividing the average laser power by the powder feed rate. The deposition efficiency was not considered in this calculation as powder loss was generally considered to take place between each deposition line, when the laser source was not emitting. The specific energy of deposition provides an indication as to which combination
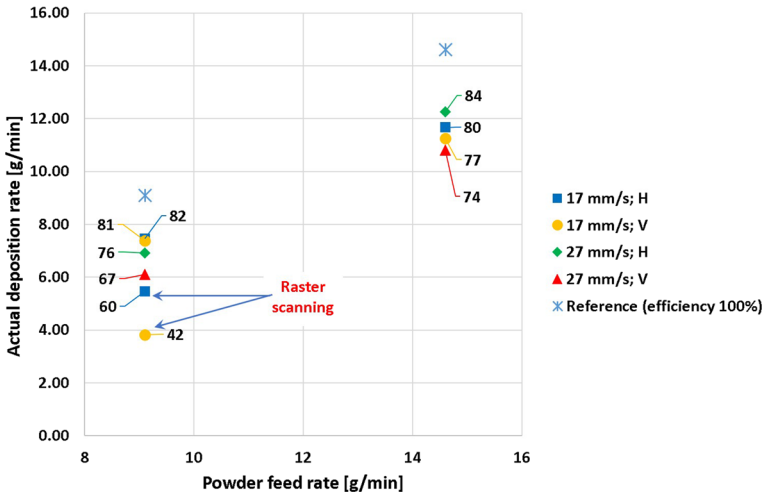
**Fig. 18** Actual deposition rate as a function of powder feed rate and scanning velocity

of process parameters leads to the most energy efficient outcomes, noting that all samples achieved consistently high density. This parameter is generally correlated to heat loss, with more limited losses leading to lower energy requirements. The specific energy of deposition therefore decreased with increasing scanning velocity, due to more limited lateral heat conduction losses, and increasing powder feed rate, due to a shorter build time. Furthermore, samples with vertical orientation required a lower specific energy of deposition due to the smaller interface with the base and therefore more limited thermal conduction losses towards the base.
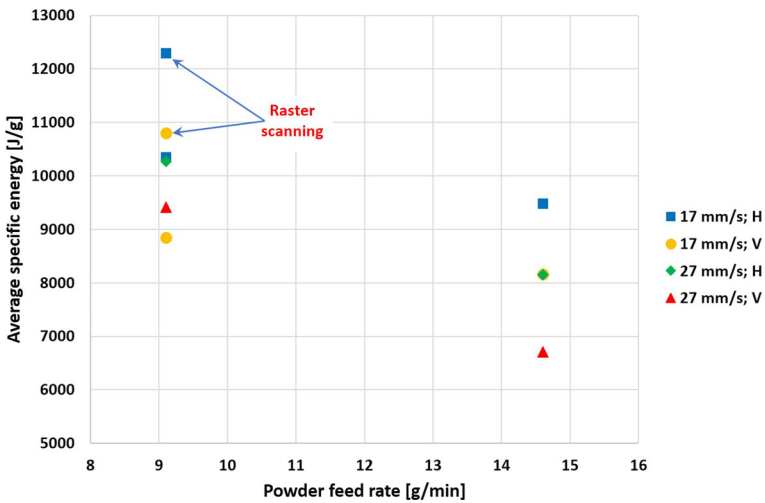


**Fig. 19** Specific energy of deposition as a function of powder feed rate and scanning velocity

## Conclusions

By investigating the effects of DED process parameters over a range in which high-density specimens were achieved, it was possible to observe important differences in terms of process outcomes and effectiveness going beyond the density. The powder line mass flow rate was found to influence the average layer height in a linear manner, while the resulting microstructure was relatively insensitive to the scanning velocity and total powder feed rate at constant powder feed per unit length. Deviation in base geometry increased with increasing powder feed per unit length due to the larger size of the melt pool during deposition, while the average areal surface roughness of surfaces perpendicular to the build plane was lower with a snake scanning strategy, lower scanning velocity and lower powder feed rate. The yield and ultimate tensile strength, while generally similar or higher than the bulk material, displayed higher values parallel to the build plane compared to the orthogonal direction. The production time per unit mass was found to be inversely proportional to the powder feed rate and deposition efficiency, while the specific energy of deposition decreased with increasing scanning velocity and powder feed rate due to a shorter build time and therefore reduced thermal conduction losses. Mostly significantly, however, deposition efficiency was strongly influence by the scanning strategy and laser off time due to continual emission of powder throughout the build, with the raster scanning strategy leading to values as low as 42 % compared to values up to 84 % with a snake scanning strategy for horizontally oriented specimens produced at high scanning speed. While surface roughness clearly improves at lower deposition rates, the specimen strength, production time and deposition efficiency all improve at higher deposition rates over the tested parameter range, suggesting that production and quality requirements are well-aligned where post-processing is foreseen.

## References

1. Tucker, T.R., Clauer, A.H., Wright, I.G., Stropki, J.T.: Laser-processed composite metal cladding for slurry erosion resistance. Thin Solid Films **118**(1), 73–84 (1984). https://doi.org/10.1016/0040-6090(84)90107-X

2. Jiang, M., Jiang, X.P., Huang, J.G., Sun, X.F., Zhang, J.S., Ge, Y.L., Hu, Z.Q.: Microstructures of laser cladded iron-, nickel- and cobalt-base coatings. Mater. Lett. **7**(12), 453–455 (1989). https://doi.org/10.1016/0167-577X(89)90051-7

3. Molian, P.A., Hualun, L.: Laser cladding of ti-6al-4v with bn for improved wear performance. Wear **130**(2), 337–352 (1989). https://doi.org/10.1016/0043-1648(89)90187-7

4. Abbas, G., West, D.R.F.: Laser surface cladding of stellite and stellite-sic composite deposits for enhanced hardness and wear. Wear **143**(2), 353–363 (1991). https://doi.org/10.1016/0043-1648(91)90106-5

5. Pei, Y.T., Ouyang, J.H., Lei, T.C., Zhou, Y.: Laser clad zro2-y2o3 ceramic/ni-base alloy composite coatings. Ceram. Int. **21**(2), 131–136 (1995). https://doi.org/10.1016/0272-8842(95)95884-K

6. Agrawal, G., Kar, A., Mazumder, J.: Theoretical studies on extended solid solubility and nonequilibrium phase diagram for nb-al alloy formed during laser cladding. Scr. Metall. Mater. **28**(11), 1453–1458 (1993). https://doi.org/10.1016/0956-716X(93)90498-H

7. Su, D., Norris, I., Peters, C., Hall, D.R., Jones, J.D.C.: In-situ laser material process monitoring using a cladding power detection technique. Opt. Lasers Eng. **18**(5), 371–376 (1993). https://doi.org/10.1016/0143-8166(93)90045-M

8.  Pustovalov, V.K., Bobuchenko, D.S.: Thermal processes in gas-powder laser cladding of metal materials. Int. J. Heat Mass Transf. **36**(9), 2449–2456 (1993). https://doi.org/10.1016/S0017-9310(05)80128-0

9.  Liu, Y., Mochel, M.E., Mazumder, J., Shibata, K.: Tem study of precipitates in laser clad ni-al bronze. Acta Metall. Mater. **42**(5), 1763–1768 (1994). https://doi.org/10.1016/0956-7151(94)90387-5

10. Yu, J., Wu, M., Wang, M.: Interfacial reactions between glass coatings and steel substrates induced by laser cladding. Surface and Coatings Technology **72**(1), 112–119 (1995). https://doi.org/10.1016/0257-8972(94)02341-7

11. Isshiki, Y., Fujiki, S., Itoh, S., Kohga, M., Hashimoto, M.: Cladding of chromium onto mild steel by low-pressure laser spraying. Thin Solid Films **288**(1), 45–49 (1996). https://doi.org/10.1016/S0040-6090(96)08793-7

12. Sallamand, P., Pelletier, J.M.: Laser cladding on aluminium-base alloys: microstructural features. Materials Science and Engineering: A **171**(1), 263–270 (1993). https://doi.org/10.1016/0921-5093(93)90414-A

13. de Damborenea, J., Vázquez, A.J., Fernández, B.: Laser-clad 316 stainless steel with ni-cr powder mixtures. Materials & Design **15**(1), 41–44 (1994). https://doi.org/10.1016/0261-3069(94)90059-0

14. de Damborenea, J., López, V., Vázquez, A.J.: Improving high-temperature oxidation of incoloy 800h by laser cladding. Surface and Coatings Technology **70**(1), 107–113 (1994). https://doi.org/10.1016/0257-8972(94)90081-7

15. Hu, Y.P., Chen, C.W., Mukherjee, K.: An analysis of powder feeding systems on quality of laser cladding. Advances in powder metallurgy and particulate materials **21**, 17–21 (1997). https://doi.org/10.1016/S0026-0657(98)80301-9

16. Lin, J., Steen, W.M.: An in-process method for the inverse estimation of the powder catchment efficiency during laser cladding. Optics & Laser Technology **30**(2), 77–84 (1998). https://doi.org/10.1016/S0030-3992(98)00007-3

17. Lin, J.: Temperature analysis of the powder streams in coaxial laser cladding. Optics & Laser Technology **31**(8), 565–570 (1999). https://doi.org/10.1016/S0030-3992(99)00115-2

18. Pei, Y.T., Hosson, J.TMD.: Functionally graded materials produced by laser cladding. Acta Mater. **48**(10), 2617–2624 (2000). https://doi.org/10.1016/S1359-6454(00)00065-3

19. Kathuria, Y.P.: Nd–yag laser cladding of cr3c2 and tic cermets. Surface and Coatings Technology **140**(3), 195–199 (2001). https://doi.org/10.1016/S0257-8972(01)01046-5

20. Barnes, S., Timms, N., Bryden, B., Pashby, I.: High power diode laser cladding. J. Mater. Process. Technol. **138**(1), 411–416 (2003). https://doi.org/10.1016/S0924-0136(03)00109-2. IMCC2000

21. Bendeich, P., Alam, N., Brandt, M., Carr, D., Short, K., Blevins, R., Curfs, C., Kirstein, O., Atkinson, G., Holden, T., Rogge, R.: Residual stress measurements in laser clad repaired low pressure turbine blades for the power industry. Materials Science and Engineering: A **437**(1), 70–74 (2006). https://doi.org/10.1016/j.msea.2006.04.065

22. Jeng, J.-Y., Lin, M.-C.: Mold fabrication and modification using hybrid processes of selective laser cladding and milling. J. Mater. Process. Technol. **110**(1), 98–103 (2001). https://doi.org/10.1016/S0924-0136(00)00850-5

23. Koch, J.L., Mazumder, J.: Rapid prototyping by laser cladding. In: International Congress on Applications of Lasers & Electro-Optics, vol. 1993:1, pp. 556–565 (1993)

24. Lewis, G.K., Milewski, J.O., Nemec, R.B., Toma, D.J., Rabe, M., Cremers, D.: Direct light fabrication, Los Alamos Laboratory Publication, LA-UR-95-2845 (1995)

25. Liu, J., Li, L.: Effects of process variables on laser direct formation of thin wall. Optics & Laser Technology **39**(2), 231–236 (2007). https://doi.org/10.1016/j.optlastec.2005.08.012

26. Lu, Z.L., Li, D.C., Lu, B.H., Zhang, A.F., Zhu, G.X., Pi, G.: The prediction of the building precision in the laser engineered net shaping process using advanced networks. Opt. Lasers Eng. **48**(5), 519–525 (2010). https://doi.org/10.1016/j.optlaseng.2010.01.002

27. Manvatkar, V.D., Gokhale, A.A., Jagan Reddy, G., Venkataramana, A., De, A.: Estimation of melt pool dimensions, thermal cycle, and hardness distribution in the laser-engineered net shaping process of austenitic stainless steel. Metall. and Mater. Trans. A. **42**(13), 4080–4087 (2011). https://doi.org/10.1007/s11661-011-0787-8

28. Wang, X., Deng, D., Hu, Y., Ning, F., Wang, H., Cong, W., Zhang, H.: Overhang structure and accuracy in laser engineered net shaping of fe-cr steel. Optics & Laser Technology **106**, 357–365 (2018). https://doi.org/10.1016/j.optlastec.2018.04.015

29. Durejko, T., Zietala, M., Polkowski, W., Czujko, T.: Thin wall tubes with fe3al/ss316l graded structure obtained by using laser engineered net shaping technology. Materials & Design **63**, 766–774 (2014). https://doi.org/10.1016/j.matdes.2014.07.011

30. de Lima, M.S.F., Sankaré, S.: Microstructure and mechanical behavior of laser additive manufactured aisi 316 stainless steel stringers. Materials & Design **55**, 526–532 (2014). https://doi.org/10.1016/j.matdes.2013.10.016

31. Yadollahi, A., Shamsaei, N., Thompson, S.M., Seely, D.W.: Effects of process time interval and heat treatment on the mechanical and microstructural properties of direct laser deposited 316l stainless steel. Materials Science and Engineering: A **644**, 171–183 (2015). https://doi.org/10.1016/j.msea.2015.07.056

32. Zhai, Y., Lados, D.A., Brown, E.J., Vigilante, G.N.: Fatigue crack growth behavior and microstructural mechanisms in ti-6al-4v manufactured by laser engineered net shaping. Int. J. Fatigue **93**, 51–63 (2016). https://doi.org/10.1016/j.ijfatigue.2016.08.009

33. Zhong, C., Gasser, A., Kittel, J., Wissenbach, K., Poprawe, R.: Improvement of material performance of inconel 718 formed by high deposition-rate laser metal deposition. Materials & Design **98**, 128–134 (2016). https://doi.org/10.1016/j.matdes.2016.03.006

34. Zietala, M., Durejko, T., Polański, M., Kunce, I., Plociński, T., Zieliński, W., Lazińska, M., Stepniowski, W., Czujko, T., Kurzydlowski, K.J., Bojar, Z.: The microstructure, mechanical properties and corrosion resistance of 316l stainless steel fabricated using laser engineered net shaping. Materials Science and Engineering: A **677**, 1–10 (2016). https://doi.org/10.1016/j.msea.2016.09.028

35. Liu, Z., Kim, H., Liu, W., Cong, W., Jiang, Q., Zhang, H.: Influence of energy density on macro/micro structures and mechanical properties of as-deposited inconel 718 parts fabricated by laser engineered net shaping. J. Manuf. Process. **42**, 96–105 (2019). https://doi.org/10.1016/j.jmapro.2019.04.020

36. Shamsaei, N., Yadollahi, A., Bian, L., Thompson, S.M.: An overview of Direct Laser Deposition for additive manufacturing; part II: Mechanical behavior, process parameter optimization and control. Additive Manufacturing **8**, 12–35 (2015). https://doi.org/10.1016/j.addma.2015.07.002

37. Nickel, A.H., Barnett, D.M., Prinz, F.B.: Thermal stresses and deposition patterns in layered manufacturing. Materials Science and Engineering: A **317**(1-2), 59–64 (2001). https://doi.org/10.1016/S0921-5093(01)01179-0

38. Kono, D., Yamaguchi, H., Oda, Y., Sakai, T.: Stabilization of standoff distance by efficient and adaptive updating of layer height command in directed energy deposition, en, CIRP J. Manuf. Sci. Technol., S175558172030064X (2020)

39. Song, L., Bagavath-Singh, V., Dutta, B., Mazumder, J.: Control of melt pool temperature and deposition height during direct metal deposition process. The International Journal of Advanced Manufacturing Technology **58**(1-4), 247–256 (2012). https://doi.org/10.1007/s00170-011-3395-2

40. Donadello, S., Motta, M., Demir, A.G., Previtali, B.: Monitoring of laser metal deposition height by means of coaxial laser triangulation. Opt. Lasers Eng. **112**, 136–144 (2019). https://doi.org/10.1016/j.optlaseng.2018.09.012

41. Ma, M., Wang, Z., Zeng, X.: A comparison on metallurgical behaviors of 316L stainless steel by selective laser melting and laser cladding deposition. Materials Science and Engineering: A **685**, 265–273 (2017). https://doi.org/10.1016/j.msea.2016.12.112

42. Zheng, B., Zhou, Y., Smugeresky, J.E., Schoenung, J.M., Lavernia, E.J.: Thermal behavior and microstructure evolution during laser deposition with laser-engineered net shaping: Part II. experimental investigation and discussion. Metall. and Mater. Trans. A. **39**(9), 2237–2245 (2008). https://doi.org/10.1007/s11661-008-9566-6

43. Saboori, A., Aversa, A., Marchese, G., Biamino, S., Lombardi, M., Fino, P.: Microstructure and mechanical properties of AISI 316L produced by Directed Energy Deposition-based additive manufacturing: A review. Appl. Sci. **10**(9), 3310 (2020). https://doi.org/10.3390/app10093310

44. Tan, Z.E., Pang, J.H.L., Kaminski, J., Pepin, H.: Characterisation of porosity, density, and microstructure of directed energy deposited stainless steel AISI 316L. Additive Manufacturing **25**, 286–296 (2019). https://doi.org/10.1016/j.addma.2018.11.014

45. Ribeiro, K.S.B., Mariani, F.E., Coelho, R.T.: A study of different deposition strategies in Direct Energy Deposition (DED) processes. Procedia Manufacturing **48**, 663–670 (2020). https://doi.org/10.1016/j.promfg.2020.05.158 (en)

46. Shim, D.-S., Baek, G.-Y., Seo, J.-S., Shin, G.-Y., Kim, K.-P., Lee, K.-Y.: Effect of layer thickness setting on deposition characteristics in direct energy deposition (DED) process. Optics & Laser Technology **86**, 69–78 (2016). https://doi.org/10.1016/j.optlastec.2016.07.001 (en)

47. Fujishima, M., Oda, Y., Ashida, R., Takezawa, K., Kondo, M.: Study on factors for pores and cladding shape in the deposition processes of Inconel 625 by the directed energy deposition (DED) method. CIRP J. Manuf. Sci. Technol. **19**, 200–204 (2017). https://doi.org/10.1016/j.cirpj.2017.04.003 (en)

48. Terrassa, K.L., Haley, J.C., MacDonald, B.E., Schoenung, J.M.: Reuse of powder feedstock for directed energy deposition. Powder Technol. **338**, 819–829 (2018). https://doi.org/10.1016/j.powtec.2018.07.065 (en)

## Affiliations

**Alessandro Ascari[1]** ⬤ **· Adrian H. A. Lutey[2] · Erica Liverani[1] · Alessandro Fortunato[1]**

Adrian H. A. Lutey
adrian.lutey@unipr.it

Erica Liverani
erica.liverani2@unibo.it

Alessandro Fortunato
alessandro.fortunato@unibo.it

[1]    Department of Industrial Engineering, University of Bologna, Viale Risorgimento, 2, Bologna, Italy

[2]    Department of Engineering and Architecture, University of Parma, Parco Area delle Scienze, 181/A, Parma, Italy